Improving dosage and timing of radiopharmaceutical therapies using computational modeling of tumor and radioligand dynamics

Elahe Mollaheydar[1,2], Babak Saboury[2,3], Arman Rahmim[2,3,4], and Eric N. Cytrynbaum[5]

[1]School of Biomedical Engineering, University of British Columbia, Vancouver, BC, Canada
[2]Department of Integrative Oncology, BC Cancer Research Institute, Vancouver, BC, Canada
[3]Institute of Nuclear Medicine, Bethesda, MD, US
[4]Departments of Radiology and Physics, University of British Columbia, Vancouver, BC, Canada
[5] Department of Mathematics, University of British Columbia, Vancouver, BC, Canada

May 23, 2025

Corresponding Author: Eric N. Cytrynbaum, Email: cytryn@math.ubc.ca

Abstract

Purpose: Radiopharmaceutical therapies (RPTs) are showing significant value in targeting various forms of cancer; meanwhile, as an emerging paradigm there is significant room for optimization of RPTs. We developed a computational model towards improving therapeutic strategies via modification of dosage and timing of RPT injections.

Methods: Our model simulates tumor growth, the pharmacokinetics of RPTs, and the radiobiological impact of radionuclide decay through energy deposition on tumor tissue. Specifically, we use the Hybrid Automata Library (HAL) to simulate tissue containing a heterogeneous tumor and its vasculature, along with oxygen and radiopharmaceutical concentration. Therapeutic interventions are modeled using a multiscale approach that connects whole-body compartmental modeling of radiopharmaceutical concentrations to the linear-quadratic survival model for tumor cells. We evaluated several treatment schedules applied to tumors with different conditions resulting in insights on how to improve RPTs.

Results: Tumors with varying vascular densities responded differently to identical therapeutic regimens. We also found that the timing and frequency of therapeutic interventions played important roles in the effectiveness of RPTs. Overall, we demonstrated that a one-size-fits-all approach is inadequate for achieving optimal therapies.

Conclusions: Our model provided insights for improving treatment schedules that highlight the potential for personalized approaches to achieve better outcomes. The code for the model is publicly available on GitHub: github.com/Elahe-hmh/HAL_RPT

Keywords: Radiopharmaceutical Therapy, Tumor Dynamics, Multiscale Modeling, Hybrid Automata Library, Therapy Optimization

Introduction

Radiopharmaceutical therapies (RPTs) are emerging as a very promising paradigm for treating various cancers by delivering targeted radiation doses to tumor cells while sparing healthy tissues [1]. RPTs rely on the unique properties of radiopharmaceuticals, consisting of a radionuclide combined with a targeting vector, such as a peptide or anti-body. These vectors selectively bind to cancer-specific markers, enabling precise delivery of cytotoxic radiation [2]. RPTs have shown significant efficacy in treating metastatic cancers [1], particularly neuroendocrine tumors and prostate cancer, as shown by successes with Lutetium-177 (Lu-177) and Actinium-225 (Ac-225) labeled therapies [3, 4, 5]. RPTs represent a paradigm shift in cancer treatment. They take advantage of the ability of radiopharmaceuticals to deliver targeted radiation doses to malignant cells with high precision. Over the past few years, RPTs have gained significant attention, particularly in the treatment of metastatic cancers, where conventional treatments may be inadequate [1, 6]. The growing body of evidence supporting the efficacy of RPTs [7, 8, 9] highlights the need for a deeper understanding of the key factors that influence treatment personalization, including adjustment of injected activity, optimization of interval scheduling, and modification of pharmacokinetics using various interventions.

The treatment schedule with RPTs is a critical factor influencing therapeutic outcomes with the half-life of the radionuclide, the pharmacokinetics of the targeting vector, and the

tumor biology all playing important roles. Fractionated dosing schedules, which involve administering multiple smaller doses over time, have been explored to enhance therapeutic efficacy while minimizing toxicity [10]. Fractionation enhances tumor uptake by promoting the resurfacing of target receptors that allow normal tissues to repair, and facilitating the reoxygenation of hypoxic tumor regions, thereby improving the overall treatment response. [11].

Personalization of RPTs involves tailoring treatment to the individual characteristics of the patient and their tumor. This approach considers factors such as tumor heterogeneity, receptor expression levels, and patient-specific pharmacokinetics. Advances in imaging and dosimetry have enabled accurate quantification of radiation dose delivered to tumors and normal tissues, paving the way for personalized treatment regimens [12, 13]. Theranostics integrates therapeutic and diagnostic capabilities into a cohesive platform, where both imaging and RPT agents have the same molecular target (e.g., the PSMA protein in prostate cancer cells) [14, 15]. Thus, it offers the potential for a personalized approach to cancer treatment [16, 17], enabling dose adjustments based on the observed tumor response, potentially improving therapeutic outcomes [18].

Computational models provide significant opportunities for optimizing RPT. These models may enable significant advancements by predicting radiation dose distributions within tumors and normal tissues, thereby refining dosing regimens and improving therapeutic outcomes. Solnes et al. [19] explored the theranostic applications of radiopharmaceuticals, emphasizing the integration of imaging and therapy to optimize treatment protocols. Similarly, Scott et al. [20] developed models to simulate dosimetry and therapeutic efficacy, contributing to the understanding of radionuclide dynamics in RPTs. Among various modeling approaches, the Cellular Automata (CA) method has emerged as a popular and effective tool in the field of cancer therapy [21, 22, 23]. Using CA, Ahn et al. [24] simulated a spatiotemporal kinetic model with cellular resolution to describe tumor heterogeneity. Rockne et al. (2009) used partial differential equations to study a spatially distributed population of glioma cells under various radiotherapy treatment schedules [25]. However, existing models have yet to address specific challenges, such as the integration of multiscale dynamics or the precise impact of vascular composition heterogeneity on therapy outcomes. Here, we address these gaps by developing a computational framework that incorporates these factors, filling in much-needed theoretical foundations for considering the interplay between pharmacokinetics, radiobiology, and tumor microenvironment to guide clinical practice toward more efficient and personalized RPT protocols.

Methods

We developed a multi-scale model for the radionuclide ^{177}Lu and the radiopharmaceutical ^{177}Lu-PSMA-617, focusing on beta-minus decay. More details are provided in the Supplemental Materials. The model simulates tumor growth and therapeutic effects through RPT dynamics, which are detailed in our study. The model can be easily extended to other radiopharmaceuticals by adjusting physical half-life as well as kinetic and radiobiological parameters.

In pharmacology language, pharmacokinetics refers to what the body does to a drug,

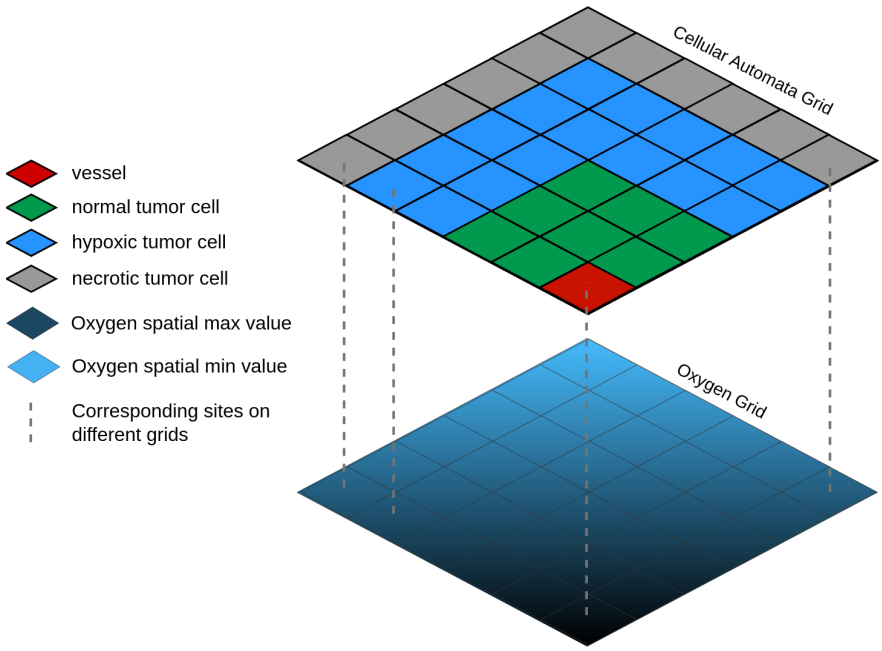

Figure 1: A diagram of the HAL domains. The top domain shows the CA grid with node states colour coded as indicated. The bottom domain shows the oxygen concentration on a similar grid, lined up with the CA grid allowing for coupling of the dynamics.

whereas pharmacodynamics refers to what the drug does to the body [26]. In RPTs, the latter occurs through radiation biophysics. As such, in what follows, we describe both the pharmacokinetic model that we use, as well as the radiation biophysics component.

At the smallest scale, the tumour itself and surrounding tissue, we used the Hybrid Automata Library (HAL) [27], a specialized Java library designed to simulate a 2D cellular-automata (CA) lattice coupled to a continuous spatial process (also in 2D) such as substrate diffusion. The CA was used to represent healthy cells, tumour cells in various discrete states, and capillaries. The continuous spatial process coupled to the CA was the diffusion and uptake of oxygen. This component of the model is illustrated in Figure 1.

The model also included a compartment submodel spanning several scales to track radiopharmaceutical concentration. Compartments included the blood, into which radiopharmaceuticals were injected, vasculature, interstitial tissue around the tumour, a bound state and an internalized state within the tumour. This component is illustrated in Figure 2.

Each CA node (we use the word node instead of cell to distinguish CA elements from biological cells) can be either a capillary, or a (biological) cell with cells taking on one of the following states: normal tumor cell, hypoxic tumour cell, necrotic tumor cell. The three tumour types are determined by the local oxygen concentration around the cell with thresholds distinguishing normal (high oxygen), hypoxic (mid-range oxygen), and necrotic (low oxygen). Normal and hypoxic cells can reproduce stochastically into neighbouring empty nodes.The simulation starts with initial tumor seed of size 1 mm and the division probability is calculated as the ratio of the oxygen level at the cell site to the oxygen level in the blood vessel, multiplied by the maximum division rate for cells . This results in higher division probabilities for normal tumor cells under normoxic conditions, while hypoxic tumor

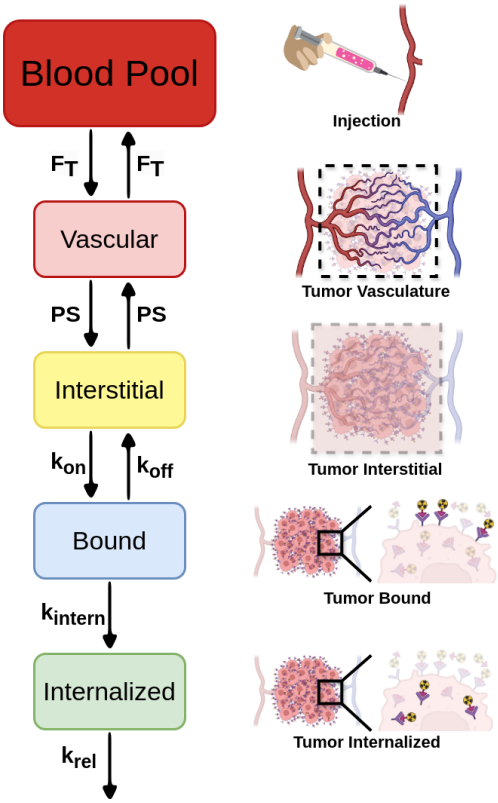

Figure 2: The compartmental submodel used to track the delivery of radiopharmaceutical to the tumour and its distribution within the tumour tissue. The model is divided into five compartments as shown. Radiopharmaceuticals are injected into the blood, from which they transfer to the vascular compartment and from there into the interstitial space. They can bind to tumor-cell receptors, entering the bound state. Subsequently, the radiopharmaceuticals can get internalized within tumor cells and may be released. The illustrations beside each compartment show an anatomical view of the compartment for clarity but the model just tracks the total radiopharmaceutical in the compartment.

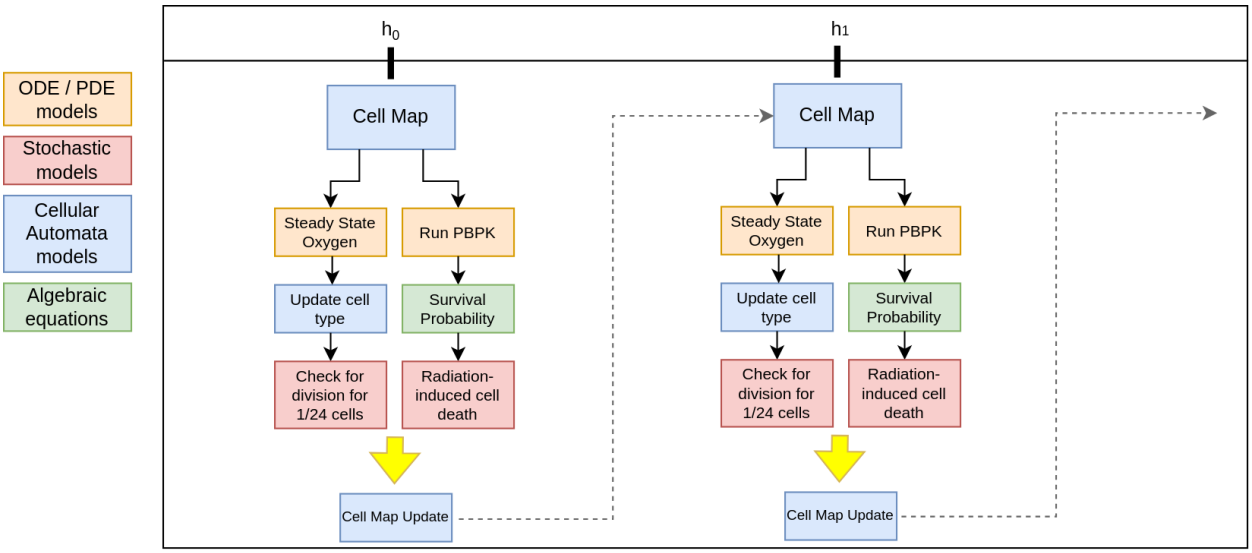

Figure 3: The outline of the steps of the simulation designed to represent tumor growth and the effects of radiopharmaceutical therapy. The model simulates the tumor microenvironment by calculating the oxygen quasi-steady-state and applying a compartmental model to track the drug distribution in the tumor. These processes result in continuous updating of cell states within the tumor for the next hour. The color of the box depicts the modeling approach for that process mentioned in the legend.

cells have reduced division probabilities due to lower oxygen levels. They can also undergo radiation-induced apoptosis and be removed leaving the node empty. Necrotic cells are dead; they do not reproduce and are incapable of converting to any of the other cell state even if oxygen increases locally.

The model (illustrated in Figure 3) allows for the simulation of various treatment schedules, examining the impact of different injection frequencies, intervals, and cumulative doses on tumor growth and cell survival with 10% specific activity (i.e., a 10% fraction of hot content) at each injection. The ^{177}Lu-PSMA-617 RPT schedules tested include:

- Therapy 1: Monthly injections cycles of equal amounts for four months with a total of 400 nmol of radiopharmaceutical.
- Therapy 2: Weekly injections of equal amounts for eight weeks with a total of 400 nmol of radiopharmaceutical.
- Therapy 3: Injections on days 5, 12, 14, and 16 of equal amounts for the same total of 400 nmol of radiopharmaceutical.
- Therapy 4: Injections on days 12, 14, 17, and 20 each with 70 nmol, an injection on day 23 of 100 nmol, and a final smaller amount of 20 nmol on day 23 for the same total amount of 400 nmol of radiopharmaceutical.
- Therapy 5: Injections on days 12, 14, 17, 20 each with 70 nmol,and two injections on days 24 and 26, each with amounts of 100 nmol, totaling 580 nmol.

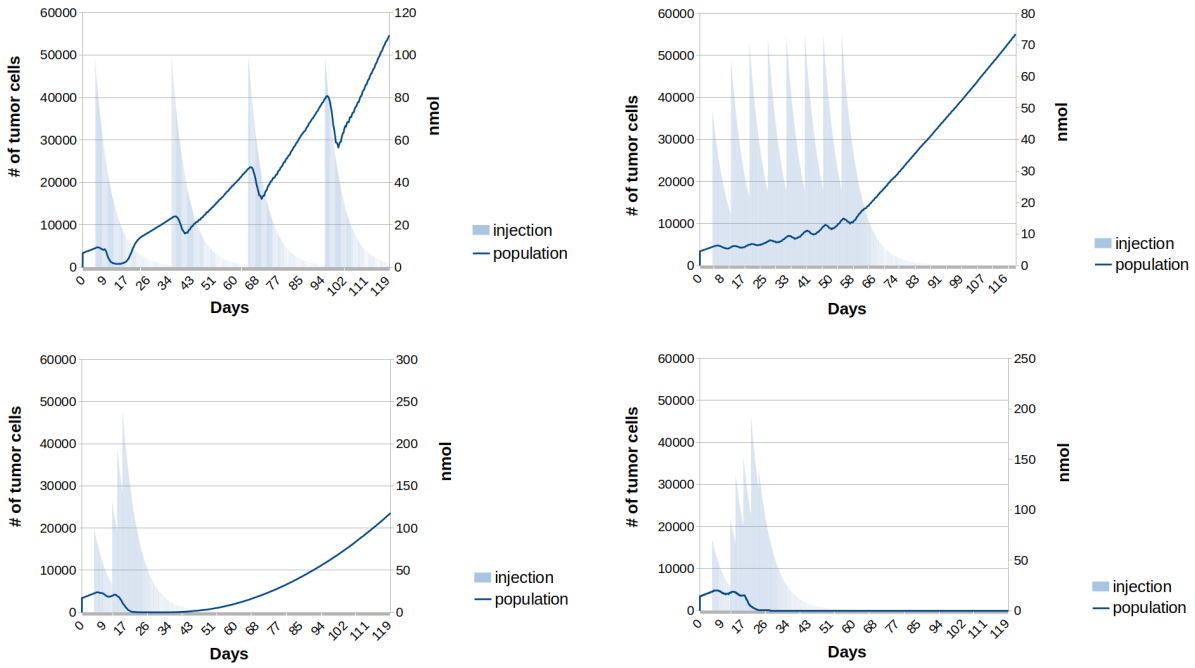

Figure 4: Effect of Therapies 1 to 4 (top left, top right, bottom left, bottom right) on the tumor with uniform high-density vasculature in the original vasculature density. The total amount of radiopharmaceutical in the blood compartment is shown with blue shading. Note that each injection adds to the existing concentration.

In Therapies 1 to 4, the total injected activity over all cycles, given above-mentioned specific activity, is about 790 mCi (29 GBq), and in Therapy 5, it is about 950 mCi (35 GBq). These specific numbers and frequencies were selected not to provide direct recommendations for clinical use. Rather, they were intended to illustrate the significance of timing and dosage in RPTs. The primary goal was thus to experiment with timing and injection quantities to observe their effects on tumor response, thereby determining the effectiveness of therapies. This underscores the role of both timing and dosage and why treatments should be personalized according to the tumor's characteristics. As such, these numbers serve as demonstrations than as established guidelines for practice.

These therapies were applied to tumors with different vascular configurations with varying vascular densities. The resulting effects on tumor growth and cell survival were analyzed to determine the influence of the RPT schedule on the outcome.

Results

We applied the model to study tumors with varying vascular densities. We considered tumors with relatively high and relatively low density of capillaries. The analysis focused on tumor growth dynamics and the response to four or five distinct RPT plans. The results for each vasculature configuration are discussed in detail below.

Figure 4 depicts the effects of the four therapies on a uniform high-density vasculature

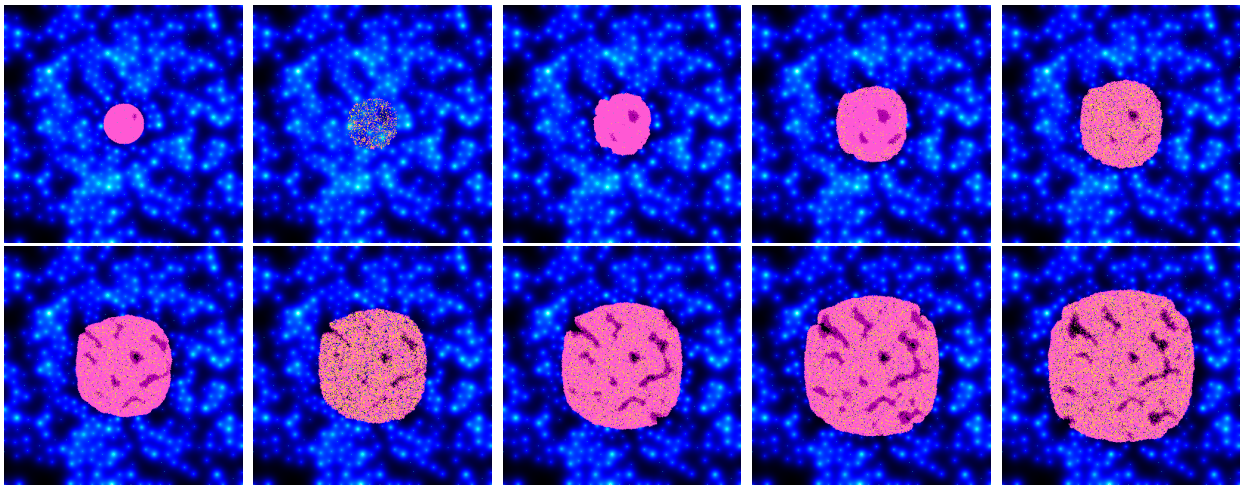

Figure 5: Effect of Therapy 1 on the tumor with uniform high-density vasculature shown at days 0, 12, 24, 36, and 48 (top row) and at days 60, 72, 84, 96, and 108 (bottom row). Normal tumor cells are shown in pink, hypoxic tumor cells in purple, necrotic tumor cells in gray, and apoptotic cells in yellow. The blue gradient indicates oxygen concentration, and the black background represents healthy tissue. Treatments occurred between the first and second panel, fourth and fifth, sixth and seventh, and ninth and tenth.

configuration. As is shown, Therapy 1 achieves some tumor cell kill, but the tumor retains its high rate of proliferation. The intervals between treatment sessions (days 5, 35, 65, and 95) are sufficiently long, allowing the tumor to compensate for cell loss and continue its growth. This therapy exhibits only a transient effect on the tumor.

Therapy 2 effectively suppresses tumor growth during the treatment period with injections administered weekly. The shorter interval (days 5, 12, 19, 26, 33, 40, 47, and 54) between sessions clearly is more effective at stopping the rapid tumor proliferation for the same total amount of radiopharmaceutical. For the time that therapy is being applied, Therapy 2 has a control effect on tumor growth bit from the time the treatment is stopped, the tumor continues its rapid proliferation.

The impact of Therapy 3 shows a significant reduction in tumor size during the initial treatment phase due to the very short intervals between administrations (days 5, 12, 14, and 16) and reduces the tumor to a few cells. However when the treatment is stopped tumor returns. This highlights the importance of the complete removal of the tumor to prevent its recovery.

Therapy 4 achieves complete tumor removal with no recurrence with the same total amount of radiopharmaceuticals. This therapy combines short intervals between initial injections (70 nmol each on days 12, 14, 17, and 20) with a larger dose (100 nmol on day 23) and a final small dose (20 nmol) to ensure the elimination of any remaining tumor cells. Figure 5 depicts the tumor and oxygen during and after Therapy 1. While only one sample is shown here, profiles for other therapies and configurations can be found in the supplementary material for further reference.

Figures 6 illustrates the effects of the five therapies on a low-density vasculature configu-

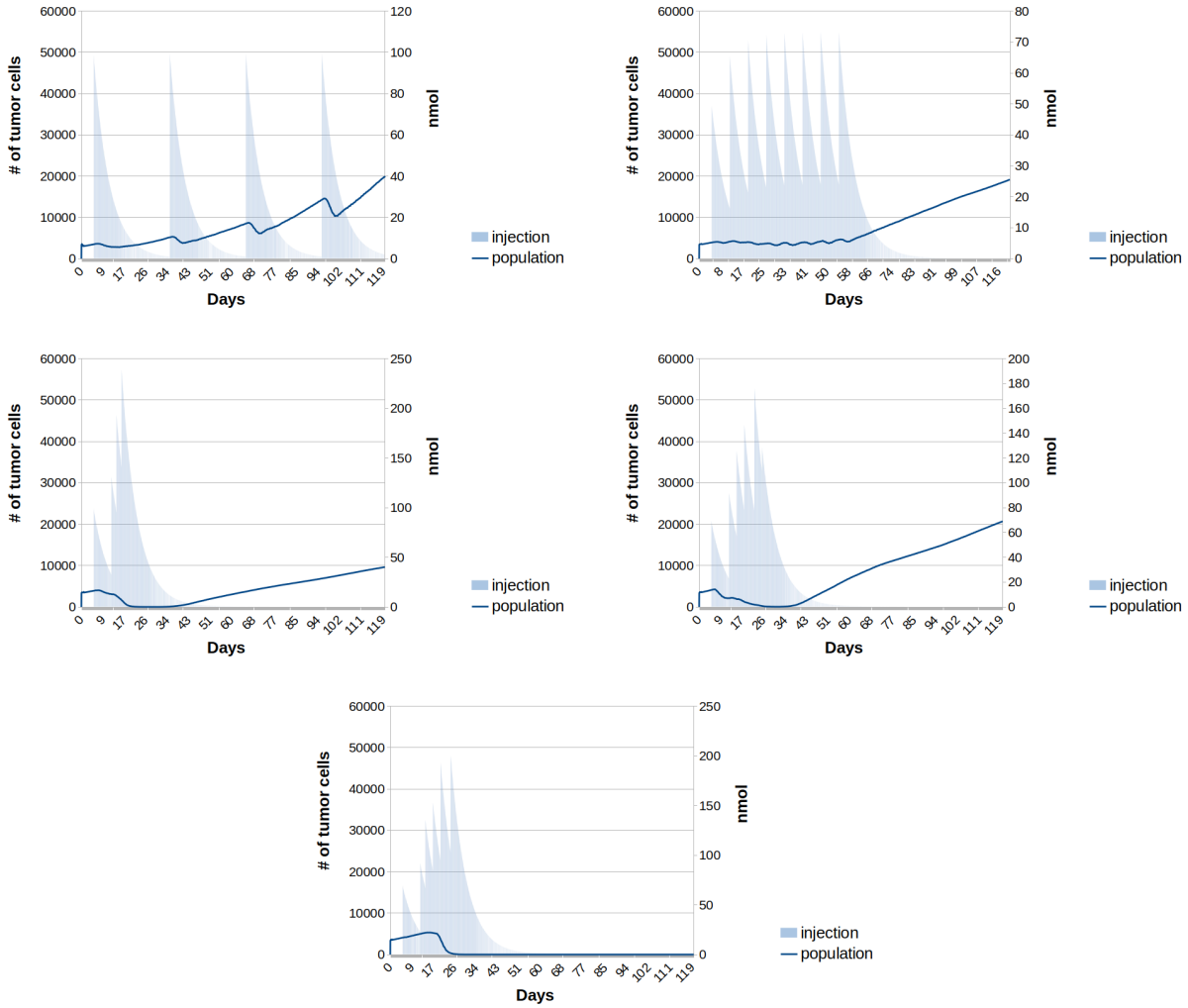

Figure 6: Effect of Therapies 1 to 5 on the tumor with uniform low-density vasculature. The total amount of radiopharmaceutical in the blood compartment is shown with blue shading. Note that each injection adds to the existing concentration.

ration, representing a sparser vascular network compared to the previous configuration. The effects of Therapies 1 and 2 were consistent with those observed in the previous vasculature conditions. Therapy 1 exhibited a transient local effect and Therapy 2 showed a transient control effect. Therapy 3 was also similar to the previous case knocking the tumor down to low cell numbers but ultimately rebounding after treatment. However, Therapy 4 was not successful in this configuration and led to tumor recurrence. The results seem to be worse than for Therapy 3

This suggests that the treatment regimens were insufficient for this highly resistant tumor pattern. To address this challenge, we introduced Therapy 5 with a different dosage and schedule. Therapy 5 used a higher dose administered over a shorter interval, unlike Therapy 4, which had a lower dose spread over a longer period. Therapy 5 was effective in this configuration too and successfully eradicated the tumor and prevented recurrence.

The results show that tumors with high vascular density were more responsive to therapy, as seen with Therapy 4 achieving complete eradication, while tumors with sparse vasculature required more intensive and higher cumulative dosing schedules to prevent recurrence. Therapies with shorter intervals between doses, such as weekly injections (Therapy 2) or frequent initial injections (Therapy 3), suppressed tumor growth more effectively during treatment but were insufficient to prevent recurrence after cessation. Therapy 5, characterized by both higher doses and short intervals, successfully eradicated tumors across all vascular profiles.

Discussion

In this work, we developed and applied a computational multiscale model that simulates the effects of various RPT regimens on a dynamic tumor. Our analysis underscores the critical role of tumor vascular density and the timing and amplitude of dosing in determining therapeutic outcomes. These findings emphasize the importance of personalized treatment planning tailored to patient-specific tumor characteristics, an already well-established idea [28, 29].

Our simulations demonstrate that tumors with varying vascular densities respond differently to identical RPT schedules. Tumors with sparse vasculature and greater treatment resistance require more aggressive treatment regimens, featuring frequent and variable dosing, to achieve effective control. Shorter intervals between injections can limit tumor recovery and repopulation, while appropriately adjusted cumulative doses increase the likelihood of complete eradication. These results support the concept that continuous therapeutic pressure is necessary to prevent tumor regrowth.

Therapeutic effects observed in this study can be categorized into four distinct outcomes: (i) therapy kills some tumor cells but tumor growth occurs throughout, (ii) therapy effectively controls tumor growth during treatment, (iii) most tumor cells are killed but residual cells lead to recurrence and (iv) therapy successfully eliminates all tumor cells. These map onto established clinical classifications as defined by RECIST criteria [30]: Progressive Disease (PD), Stable Disease (SD), Partial Response (PR), and Complete Response (CR). The interplay between the tumor growth rate and the treatment-induced killing rate is central to these outcomes. When tumor proliferation exceeds cell kill, growth persists; conversely, when therapeutic pressure dominates, tumor burden can be controlled or eliminated. This dynamic

is nonlinear and depends on factors such as vascular architecture, immune interactions, and therapy parameters like dose and frequency.

Quantifying these effective rates is challenging, as they emerge from complex biological interactions and treatment schedules. Simulation-based approaches are particularly well-suited for probing these nonlinear relationships. Studies have emphasized the influence of the tumor microenvironment on growth dynamics. Hanahan and Weinberg's work on cancer hallmarks highlights factors affecting tumor growth rate [31]. Radiobiological considerations, such as dose fractionation and sublethal damage repair, also affect RPT efficacy and must be accounted for in realistic models [32].

Our model enables this level of investigation, contributing to a growing body of work using mathematical and computational modeling to understand therapy response in nuclear oncology [33, 34, 35]. By simulating diverse tumor configurations and treatment regimens, we provide evidence that fixed-injected-activity RPT approaches may result in suboptimal outcomes due to their failure to account for patient-specific biology [36, 37].

The importance of vascular density is further illustrated in our results: Therapy 4, for instance, achieved complete tumor eradication in well-vascularized tumors but failed in poorly perfused cases, resulting in recurrence [38, 39, 40, 41]. These findings reinforce the value of individualized planning and adaptive treatment strategies. To maximize efficacy while safeguarding healthy tissue, especially organs at risk, therapy must apply sustained pressure through carefully optimized cumulative dose and injection frequency [42].

Looking ahead, the flexibility of our modular framework enables the integration of additional biological complexity. Improved modeling of the radiobiology of RPTs would be valuable [43]. An improved model should explicity incorporate processes such as DNA damage and repair as an extension of our model, in which damage and repair processes are encapsulated by the LQ model. The LQ model is well suited to external beam radiation, where the time scales of damage and repair are well-separated but for RPT these processes are temporally interleaved potentially leading to more complicated and subtle dynamics. In addition, integration of physiologically based pharmacokinetic (PBPK) models can enhance prediction of systemic drug distribution and uptake in both tumors and healthy organs [44, 45, 46].

Moreover, coupling this framework with real-time clinical data could enable the implementation of adaptive RPT strategies aligned with the emerging concept of theranostic digital twins [47, 48]. These virtual counterparts of patients could facilitate treatment optimization in silico, improving responsiveness to individual tumor evolution and patient-specific pharmacokinetics. Finally, this model opens the door to exploring combination therapies, such as RPTs with chemotherapy or immunotherapy, which may yield synergistic effects. Simulating these approaches across tumor types could identify more effective, personalized strategies and inform rational clinical trial designs.

In conclusion, our study highlights the importance of computational modeling in advancing precision medicine in nuclear oncology. Our findings reinforce the need for individualized treatment planning based on tumor biology, and our flexible modeling platform lays the foundation for future innovations in adaptive, data-driven cancer therapy.

Acknowledgements

We acknowledge funding support by the IAEA Marie Sklodowska-Curie Fellowship Programme (MSCFP) scholarship, the BC Cancer Foundation, Networking Health Ltd., and the Canadian Institutes of Health Research (CIHR) Project Grant PJT-162216.

Conflict of Interest

The authors declare that they have no conflicts of interest related to this study.

References

[1] George Sgouros, Lisa Bodei, Michael R McDevitt, and Jessie R Nedrow. Radiopharmaceutical therapy in cancer: clinical advances and challenges. *Nat. Rev. Drug Discov.*, 19(9):589–608, September 2020.

[2] Ashutosh Dash, Sudipta Chakraborty, Maroor Raghavan Ambikalmajan Pillai, and Furn F Russ Knapp, Jr. Peptide receptor radionuclide therapy: an overview. *Cancer Biother. Radiopharm.*, 30(2):47–71, March 2015.

[3] Wolfgang P Fendler, Jeremie Calais, Martin Allen-Auerbach, Johannes Gartmann, Ramina Juarez, Fiona I Chu, Nicholas G Nickols, Robert E Reiter, Matthew B Rettig, and Johannes Czernin. The evolving role of psma-pet imaging in initial staging and therapy response assessment for prostate cancer. *Nature Reviews Urology*, 18(9):510–525, 2021.

[4] Rodney J Hicks. The evolving role of molecular imaging in guiding more effective cancer therapy. *The oncologist*, 22(5):450–458, 2017.

[5] Clemens Kratochwil, Frederik L Giesel, Margarita Stefanova, Martina Benesova, Markus Bronzel, Ali Afshar-Oromieh, Walter Mier, Matthias Eder, Klaus Kopka, and Uwe Haberkorn. Targeted alpha therapy of metastatic castration-resistant prostate cancer with 225ac-psma-617: dosimetry estimate and empiric dose finding. *Journal of nuclear medicine*, 58(10):1624–1631, 2017.

[6] Aidan Healy, Elaine Ho, Phillip Kuo, and Katherine Zukotynski. A brief overview of targeted radionuclide therapy trials in 2022. *Front. Nucl. Med.*, 3:1169650, June 2023.

[7] J.J. Rosales, M.L. Domínguez, L. Sancho, E. Prieto, M. de Arcocha, I. Torres, A. Roteta, R. Ramos, and G. Quincoces. State of the art and future perspectives of new radionuclides in nuclear medicine. *Revista Española de Medicina Nuclear e Imagen Molecular (English Edition)*, 44(1):500082, 2025.

[8] Siju C George and E James Jebaseelan Samuel. Developments in 177Lu-based radiopharmaceutical therapy and dosimetry. *Front. Chem.*, 11:1218670, July 2023.

[9] Keamogetswe Ramonaheng, Milani Qebetu, Honest Ndlovu, Cecile Swanepoel, Liani Smith, Sipho Mdanda, Amanda Mdlophane, and Mike Sathekge. Activity quantification and dosimetry in radiopharmaceutical therapy with reference to 177Lutetium. *Front. Nucl. Med.*, 4:1355912, March 2024.

[10] S. Renee Campbell, J. Devin Kuehne, Caroline Foster, Ben C Schneider, Delphine Denoyer, Katherine A Selting, Peter Laverman, and Bart Cornelissen. Personalizing radiopharmaceutical therapies: integrating the clinic and the laboratory. *EJNMMI Research*, 10:1–14, 2020.

[11] Lisa Bodei, Dik J Kwekkeboom, Mark Kidd, and Irvin M Modlin. Redefining optimal peptide receptor radionuclide therapy dosing: a rising issue. *European journal of nuclear medicine and molecular imaging*, 43:1–3, 2016.

[12] Christopher J Anderson. Theranostics: The future of precision medicine. *Proceedings of the National Academy of Sciences*, 118(24):e2026844118, 2021.

[13] Cornelius M Zechmann, Ali Afshar-Oromieh, Thomas Armor, Florian Spohn, Jürgen Debus, Uwe Haberkorn, and Walter Mier. Personalized treatment and personalized dosimetry in prostate cancer care. *The Prostate*, 74(16):1568–1578, 2014.

[14] Andrea Farolfi, Wolfgang Fendler, Amir Iravani, Uwe Haberkorn, Rodney Hicks, Ken Herrmann, Jochen Walz, and Stefano Fanti. Theranostics for advanced prostate cancer: Current indications and future developments. *Eur. Urol. Oncol.*, 2(2):152–162, March 2019.

[15] Chalermrat Kaewput and Sobhan Vinjamuri. Update of PSMA theranostics in prostate cancer: Current applications and future trends. *J. Clin. Med.*, 11(10):2738, May 2022.

[16] Jean-Francois Chatal, C Albert Hoefnagel, and Claude F Meares. From diagnostic to therapeutic radiopharmaceuticals. *Journal of Nuclear Medicine*, 55(2):193–202, 2014.

[17] Gunther von Amsberg, Konrad Steinestel, Laura Zabel, Andreas Winter, Claudia Eichelberg, Jens Bedke, Ulrich Wetterauer, Luise Rossius, Michael Rink, Anna Roosen, et al. A roadmap for the clinical implementation of theranostics in oncology. *Oncotarget*, 9(26):18252, 2018.

[18] Karen Chen and Xiaoyuan Chen. Theranostic imaging of the tumor microenvironment. *Advanced drug delivery reviews*, 113:7–11, 2016.

[19] Lilja B Solnes, Marc Pantel, Morgan R Villalobos, Laura M Carter, Michele Spaliviero, Heiko Schoder, and Neeta Pandit-Taskar. Theranostic applications of radiopharmaceuticals in precision oncology: the role of molecular imaging in optimizing therapy. *Journal of Nuclear Medicine*, 59(3):414–419, 2018.

[20] Aaron M Scott, Katherine L Zakian, Bobby A Parker, Hanna Koprowski, and Zhuo Cheng. Modeling and simulation in radiopharmaceutical therapy: Predicting dosimetry, efficacy, and toxicity. *Frontiers in Oncology*, 10:543, 2020.

[21] B Ribba, T Alarcón, K Marron, P K Maini, and Z Agur. The use of hybrid cellular automaton models for improving cancer therapy. In *Lecture Notes in Computer Science*, Lecture notes in computer science, pages 444–453. Springer Berlin Heidelberg, Berlin, Heidelberg, 2004.

[22] Shiva Shahmoradi, Fereidoun Nowshiravan Rahatabad, and Keivan Maghooli. A stochastic cellular automata model of growth of avascular tumor with immune response and immunotherapy. *Inform. Med. Unlocked*, 12:81–87, January 2018.

[23] Fateme Pourhasanzade and S H Sabzpoushan. A cellular automata model of chemotherapy effects on tumour growth: targeting cancer and immune cells. *Math. Comput. Model. Dyn. Syst.*, 25(1):63–89, January 2019.

[24] Hailey S H Ahn, Yas Oloumi Yazdi, Brennan J Wadsworth, K Bennewith, Arman Rahmim, and I Klyuzhin. Relating macroscopic PET radiomics features to microscopic tumor phenotypes using a stochastic mathematical model of cellular metabolism and proliferation. *Cancers (Basel)*, 16(12):2215, June 2024.

[25] Russell Rockne, Ellsworth C Alvord, Jason K Rockhill, and Kristin R Swanson. A mathematical model for brain tumor response to radiation therapy. *Journal of mathematical biology*, 58:561–578, 2009.

[26] Open Resources for Nursing (Open RN), Kimberly Ernstmeyer, and Elizabeth Christman. Chapter 1 pharmacokinetics & pharmacodynamics. In *Nursing Pharmacology [Internet]. 2nd edition*. Chippewa Valley Technical College, 2023.

[27] Rafael R Bravo, Etienne Baratchart, Jeffrey West, Ryan O Schenck, Anna K Miller, Jill Gallaher, Chandler D Gatenbee, David Basanta, Mark Robertson-Tessi, and Alexander RA Anderson. Hybrid automata library: A flexible platform for hybrid modeling with real-time visualization. *PLoS computational biology*, 16(3):e1007635, 2020.

[28] Beilei Liu, Hongyu Zhou, Licheng Tan, Kin To Hugo Siu, and Xin-Yuan Guan. Exploring treatment options in cancer: Tumor treatment strategies. *Signal Transduction and Targeted Therapy*, 9(1):175, 2024.

[29] Arman Rahmim, Julia Brosch-Lenz, Ali Fele-Paranj, Fereshteh Yousefirizi, Madjid Soltani, Carlos Uribe, and Babak Saboury. Theranostic digital twins for personalized radiopharmaceutical therapies: Reimagining theranostics via computational nuclear oncology. *Frontiers in oncology*, 12:1062592, 2022.

[30] Elizabeth A Eisenhauer, Patrick Therasse, Jan Bogaerts, Lawrence H Schwartz, Danielle Sargent, Robert Ford, Janet Dancey, S Arbuck, Steve Gwyther, Margaret Mooney, et al. New response evaluation criteria in solid tumours: revised recist guideline (version 1.1). *European journal of cancer*, 45(2):228–247, 2009.

[31] Douglas Hanahan and Robert A Weinberg. Hallmarks of cancer: the next generation. *cell*, 144(5):646–674, 2011.

[32] Michael C Joiner, Albert J van der Kogel, and G Gordon Steel. Introduction: the significance of radiobiology and radiotherapy for cancer treatment. In *Basic clinical radiobiology*, pages 1–8. CRC Press, 2018.

[33] Tahir Yusufaly, Emilie Roncali, Julia Brosch-Lenz, Carlos Uribe, Abhinav K Jha, Geoffrey Currie, Joyita Dutta, Georges El-Fakhri, Helena McMeekin, Neeta Pandit-Taskar, Jazmin Schwartz, Kuangyu Shi, Lidia Strigari, Habib Zaidi, Babak Saboury, and Arman Rahmim. Computational nuclear oncology toward precision radiopharmaceutical therapies: Current tools, techniques, and uncharted territories. *J. Nucl. Med.*, February 2025.

[34] Lidia Strigari, Jazmin Schwarz, Tyler Bradshaw, Julia Brosch-Lenz, Geoffrey Currie, Georges El-Fakhri, Abhinav K Jha, Signe Mežinska, Neeta Pandit-Taskar, Emilie Roncali, Kuangyu Shi, Carlos Uribe, Tahir Yusufaly, Habib Zaidi, Arman Rahmim, and Babak Saboury. Computational nuclear oncology toward precision radiopharmaceutical therapies: Ethical, regulatory, and socioeconomic dimensions of theranostic digital twins. *J. Nucl. Med.*, January 2025.

[35] Nouran R R Zaid, Remco Bastiaannet, Rob Hobbs, and George Sgouros. Mathematic modeling of tumor growth during [177lu]lu-PSMA therapy: Insights into treatment optimization. *J. Nucl. Med.*, 66(1):84–90, January 2025.

[36] Siju C George and E James Jebaseelan Samuel. Developments in 177lu-based radiopharmaceutical therapy and dosimetry. *Frontiers in Chemistry*, 11:1218670, 2023.

[37] Neeta Pandit-Taskar, Amir Iravani, Dan Lee, Heather Jacene, Dan Pryma, Thomas Hope, Babak Saboury, Jacek Capala, and Richard L Wahl. Dosimetry in clinical radiopharmaceutical therapy of cancer: practicality versus perfection in current practice. *Journal of Nuclear Medicine*, 62(Supplement 3):60S–72S, 2021.

[38] Anahita Piranfar, Mohammad Souri, Arman Rahmim, and Madjid Soltani. Localized radiotherapy of solid tumors using radiopharmaceutical loaded implantable system: insights from a mathematical model. *Front. Oncol.*, 14:1320371, February 2024.

[39] Nathaniel Braman, Prateek Prasanna, Kaustav Bera, Mehdi Alilou, Mohammadhadi Khorrami, Patrick Leo, Maryam Etesami, Manasa Vulchi, Paulette Turk, Amit Gupta, Prantesh Jain, Pingfu Fu, Nathan Pennell, Vamsidhar Velcheti, Jame Abraham, Donna Plecha, and Anant Madabhushi. Novel radiomic measurements of tumor- associated vasculature morphology on clinical imaging as a biomarker of treatment response in multiple cancers. *arXiv [q-bio.QM]*, October 2022.

[40] Mohammad Amin Abazari, M Soltani, Faezeh Eydi, Arman Rahmim, and Farshad Moradi Kashkooli. Mathematical modeling of ^{18}F-fluoromisonidazole (^{18}F-FMISO) radiopharmaceutical transport in vascularized solid tumors. *arXiv [physics.bio-ph]*, May 2024.

[41] Navid Mohammad Mirzaei, Panayotis G Kevrekidis, and Leili Shahriyari. Oxygen, angiogenesis, cancer and immune interplay in breast tumor micro-environment: A computational investigation. *arXiv [q-bio.QM]*, April 2024.

[42] Jay Jasti, Hua Zhong, Vandana Panwar, Vipul Jarmale, Jeffrey Miyata, Deyssy Carrillo, Alana Christie, Dinesh Rakheja, Zora Modrusan, Edward Ernest Kadel, III, Niha Beig, Mahrukh Huseni, James Brugarolas, Payal Kapur, and Satwik Rajaram. Histopathology based AI model predicts anti-angiogenic therapy response in renal cancer clinical trial. *arXiv [q-bio.QM]*, May 2024.

[43] Hamid Abdollahi, Babak Saboury, Tahir Yusufaly, Ian Alberts, Carlos Uribe, and Arman Rahmim. Shifting the spotlight to low dose rate radiobiology in radiopharmaceutical therapies: Mathematical modelling, challenges and future directions. *IEEE Transactions on Radiation and Plasma Medical Sciences*, 2025.

[44] Nusrat J Begum, Gerhard Glatting, Hans-Jürgen Wester, Matthias Eiber, Ambros J Beer, and Peter Kletting. The effect of ligand amount, affinity and internalization on PSMA-targeted imaging and therapy: A simulation study using a PBPK model. *Sci. Rep.*, 9(1):20041, December 2019.

[45] Deni Hardiansyah, Wei Guo, Ali Asgar Attarwala, Peter Kletting, Felix M Mottaghy, and Gerhard Glatting. Treatment planning in PRRT based on simulated PET data and a PBPK model. determination of accuracy using a PET noise model: Determination of accuracy using a PET noise model. *Nuklearmedizin*, 56(1):23–30, February 2017.

[46] Ali Fele-Paranj, Babak Saboury, Carlos Uribe, and Arman Rahmim. Physiologically based radiopharmacokinetic (PBRPK) modeling to simulate and analyze radiopharmaceutical therapies: studies of non-linearities, multi-bolus injections, and albumin binding. *EJNMMI Radiopharm. Chem.*, 9(1):6, January 2024.

[47] Hamid Abdollahi, Fereshteh Yousefirizi, Isaac Shiri, Julia Brosch-Lenz, Elahe Mollaheydar, Ali Fele-Paranj, Kuangyu Shi, Habib Zaidi, Ian Alberts, Madjid Soltani, Carlos Uribe, Babak Saboury, and Arman Rahmim. Theranostic digital twins: Concept, framework and roadmap towards personalized radiopharmaceutical therapies. *Theranostics*, 14(9):3404–3422, May 2024.

[48] Julia Brosch-Lenz, Carlos Uribe, Arman Rahmim, and Babak Saboury. Theranostic digital twins: An indispensable prerequisite for personalized cancer care. *J. Nucl. Med.*, 64(3):501, March 2023.

Electronic Supplementary Materials

Supplementary Materials

This section provides detailed explanations and additional insights supporting the main findings and multiscale modeling framework used in this study. It covers the modeling of oxygen dynamics in tumor tissue (0.1), The way we used Finite State Machine to govern all cell state transitions (0.2), and the compartmental modeling approach for radiopharmaceutical distribution (0.3). Additionaly the derivation of the Lea-Catcheside factor for quantification of the radiobiological response is presented in 0.4.

0.1 Modeling Oxygen

Oxygen distribution in tumor tissues is heterogeneous due to the irregular vasculature and varying metabolic demands of different cell types [1]. This heterogeneity significantly impacts tumor growth, progression, and response to therapies [2] [3].

Oxygen concentration satisfies the diffusion equation with capillary nodes acting as sources and all cells except necrotic ones acting as sinks. The different cell types consume oxygen at different rates with normal tumour cells consuming the most, then hypoxic, then healthy and finally no consumption by necrotic cells. Because of our interest in the slower time scales in the system, oxygen is taken to be in quasi-steady state.

The partial differential equation is given by:

$$\frac{\partial u}{\partial t} = D_{O_2} \nabla^2 u - \alpha u \tag{1}$$

where u represents the oxygen concentration, D_{O_2} is the diffusion coefficient of oxygen and α is the oxygen consumption rate by the cells. This equation captures the balance between oxygen supply through diffusion and its consumption by cellular metabolic processes .

The effective consumption rate α is calculated by averaging the consumption rates of all cell types within the neighbourhood of each vessel. This involves summing the contributions from different cell types and normalizing by the population of cells, So we have an effective consumption rate for that vessel.

The consumption rates and the oxygen diffusion coefficient for the various cell types are shown in the table below.

Model parameters	Values
Oxygen diffusion	$1.65 \times 10^{-5} cm^2/s$ [4]
Normal tumor cell O_2 consumption	$4 \times 10^{-15} mol/min/cell$ [5]
Hypoxic tumor cell O_2 consumption	$2 \times 10^{-15} mol/min/cell$ [6]
Healthy cell O_2 consumption	$2.5 \times 10^{-18} mol/min/cell$ [7]

Given the relatively fast diffusion time scale of oxygen compared to the slower time scales of the model like cell death, division and therapy, we can assume that oxygen has reached a steady-state between each update of cell states.This assumption simplifies the problem by allowing us to solve for the steady-state oxygen distribution rather than solving the full time-dependent PDE [8].

To understand the steady-state solution, consider a one-dimensional radial domain with the following boundary conditions:

- A Dirichlet boundary condition at the origin, representing a vessel where $u(0) = 1$
- A Dirichlet boundary condition at infinity, representing the baseline oxygen concentration far from the vessel

Setting the time derivation equal to zero, we obtain the steady-state equation:

$$\frac{d^2u}{dx^2} = \frac{\alpha}{D_{O_2}}u, \tag{2}$$

with the boundary conditions:

$$u(0) = 1, \quad u(\infty) = 0$$

The solution to this differential equation is:

$$u(x) = e^{-kx},$$

where $k = \sqrt{\frac{\alpha}{D_{O_2}}}$ is the decay constant.

This solution is used as a kernel for the steady-state oxygen distribution around each vessel in the model where the one dimensional x variable represents radial distance from the vessel. So The oxygen concentration at each point in the oxygen grid is updated according to the steady-state solution where the distance from the vessel and the local effective consumption rate are used to determine the concentration. The concentration of oxygen in blood vessels is considered to be 100 mmHg.

0.2 Finite State Machine

The transition between cell states in the model is governed by a Finite State Machine (FSM). Finite State Machines are widely used in computational biology to model complex biological processes due to their simplicity and effectiveness in representing state transitions based on specific inputs or conditions. This is an approach to model a system that has limited number of available states. It starts in one specific state and can change from one state to another in response to certain inputs or conditions. These changes, are called transitions and is often visualized as a diagram with circles representing states and arrows representing transitions between those states. [9]

In our model, each cell operates as an individual FSM, transitioning between cell types (such as normoxic, hypoxic, and necrotic) and between alive or dead states that allows for precise control over cell behavior based on the microenvironmental conditions.

To outline the steps, we define $S_{ij}(t_n)$ to be the state of each node in the CA (at position (i, j)) at time t_n. $S_{ij}(t_n)$ can take values between 0 and 6 (corresponding to a capillary, empty, etc.). The radiopharmaceutical totals in each compartment are denoted by the vector $\bar{N}(t_n)$ in $\mathbb{R}^5$. Because oxygen is in quasi-steady state (QSS), we can calculate it at each time step from $S_{ij}(t_n)$. That means $S_{ij}(t_n)$ and $\bar{N}(t_n)$ fully specify the state of the system. The algorithm starts with calculating the QSS oxygen distribution $O_{ij}(t_n)$ from the current $S_{ij}(t_n)$ and updating the radiopharmaceutical totals by numerically integrating the radiopharmaceutical system of ODEs to get $\bar{N}(t_{n+1})$. The tumour cell types are then updated

based on the local oxygen concentration giving a temporary $S_{ij}(t'_n)$. Next come the stochastic steps of cell reproduction and radiation-induced death from which we can update the nodes again to get $S_{ij}(t_{n+1})$. This completes a single step of the algorithm; this is iterated for a specified period of time.

FSM checks the current oxygen levels at each time step to determine if a cell should remain in its current state or transition to another state, such as from a normal cell to a hypoxic cell under low oxygen conditions or reverse. It also handles the transition to dead states by evaluating the transition probabilities into oxygen induced death (necrosis) or radiation induced death (apoptosis).

After determining whether the cell stays alive or dies, the FSM calculates the division probability of the alive cells (normal and hypoxic tumor cells) along with the removal probability of the dead cells. The big picture of the FSM module is depicted in figure S1.

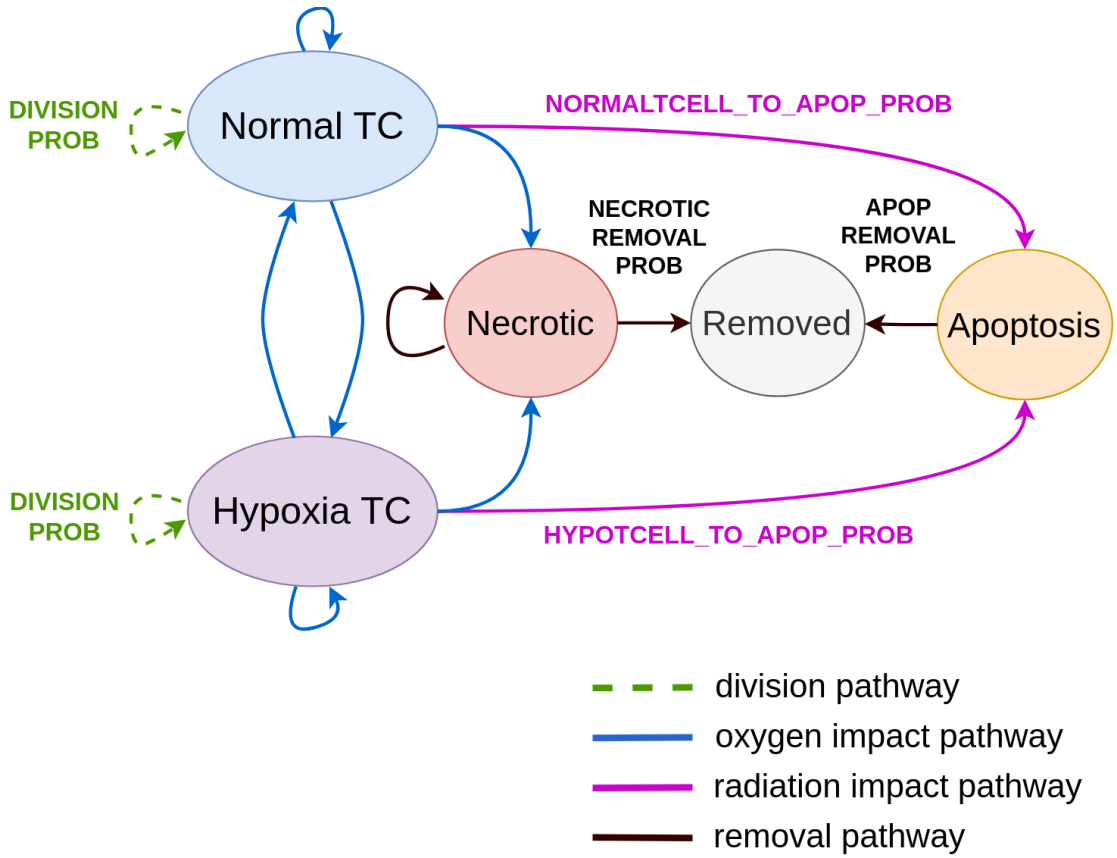

Figure S1: This figure illustrates the finite state machine governing tumor cell dynamics, showing the probabilistic transitions between cell states influenced by different factors. Normal Tumor Cells (Normal TC) and Hypoxic Tumor Cells (Hypoxia TC) can undergo division (green dashed arrows) and transition to Necrotic or Hypoxic states due to oxygen deprivation (blue arrows) or radiation induces apoptosis (purple arrows). Necrotic cells can either remain necrotic or be removed (brown arrows).

The dynamics of the cells that the FSM handles in the model, including cell types, cell

division, cell death, and cell removal, represent several cell behaviors that each need to be modeled and determined separately. We'll go into the details of each part and discuss how we model them.

0.2.1 Cell Types

As mentioned in the oxygen dynamics section, cell types are updated based on the local oxygen level at each grid site. The model includes several cell types: Normoxic tumor cells that have sufficient oxygen and remain in a normal state as "normal tumor cells", "hypoxic tumor cell" that are results of reduced oxygen levels, and "necrotic tumor cells" caused by extremely low oxygen levels, that are considered as a type of dead cell. There are two thresholds for oxygen that determine whether a cell's type will change or not.

- Hypoxia Threshold: 10 mmHg
- Necrotic Threshold: 2 mmHg

If the level of oxygen drops bellow the necrotic threshold, the cell becomes necrotic, if it drops bellow the hypoxia threshold, the cell will be hypoxic and if the oxygen level is above them, the cell will continue to live as a normal tumor cell. Of course there is a spectrum for hypoxia but in this model we consider 2 mmHg as severe hypoxia threshold named as necrosis and 10 mmHg as normal to hypoxic threshold [10] [11] [12]. Different cell types have different behaviours in terms of proliferation, resistance to drug and oxygen consumption that each will be covered in their respective sections.

0.3 Compartmental Modeling

The pharmacokinetics (drug delivery) of the model are handled using a well-mixed-compartment model consisting of five ODEs for the total amount of radiopharmaceutical found in each of the relevant compartments: body vasculature, capillaries in the tumour, tumour interstitium, bound to tumour cells, and internalized within tumour cells. Although radiopharmaceutical could be treated similarly to oxygen within the tumour, we do not track it spatially but instead treat radiopharmaceutical concentration as residing in well-mixed compartments, specifically the interstitial, bound, and internalized compartments, illustrated in Fig. 2. We justify this choice because the typical distance traveled by the emitted particles (beta) is not small compared to the diameter of the tumours considered. Thus, in a spatial model, any spatial inhomogeneity in the radiopharmaceutical distribution would get convolved with a broad kernel to get the distribution of radiation delivery. This smoothing suggests that it is not critical to model the spatial distribution of radiopharmaceuticals at this timesacale and spatial scale we are modeling.

The compartmental approach used in here is a 4-Tissue 5-Compartment model that includes four tissue compartments and an additional compartment typically representing the blood. The radiodrug is injected into the blood stream, from where it travels through the body and tumor tissue, then moves between tumor different compartments. To describe the dynamic of the drug in these compartments we use system of Ordinary Differential Equations

(ODEs) where each equation tracks the number of drug molecules in each compartment. The system is expressed as bellow:

$$
\begin{aligned}
\frac{dN_{BP}}{dt} &= -\lambda_{bio} N_{BP}, \\
\frac{dN_v}{dt} &= F_T(\frac{N_{BP}}{V_{BP}} - \frac{N_v}{V_v}) + PS(\frac{N_{int}}{V_{int}} - \frac{N_v}{V_v}) \\
\frac{dN_{int}}{dt} &= -PS(\frac{N_{int}}{V_{int}} - \frac{N_v}{V_v}) - \frac{k_{on} N_{int}}{V_{int}}(R_0 - N_b) + k_{off} N_b \\
\frac{dN_b}{dt} &= \frac{k_{on} N_{int}}{V_{int}}(R_0 - N_b) - k_{off} N_b - k_{intern} N_b \\
\frac{N_{intern}}{dt} &= k_{intern} N_b - k_{rel} N_{intern}
\end{aligned}
$$

where:

N_{BP} : Number of drug molecules in blood compartment
N_v : Number of drug molecules in vascular compartment
N_{int} : Number of drug molecules in interstitial compartment
N_b : Number of drug molecules in bound compartment
N_{intern} : Number of drug molecules in internalized compartment
λ_{bio} : Biological half-life
F_T : The flow between tumor vasculature and the rest of the body
PS : Permeability rate between vasculature and interstitial space
V_{BP} : Volume of the blood pool
V_v : Volume of the tumor vascular compartment
V_{int} : Volume of the tumor interstitial space
k_{on} : Binding rate
k_{off} : Unbinding rate
k_{intern} : Internalization rate
k_{rel} : Release rate
R_0 : Number of receptors in tumor tissue

We can re-write the system using the concentrations:

$$
\begin{aligned}
\frac{dC_{BP}}{dt} &= -\lambda_{bio} C_{BP}, \\
\frac{dC_v}{dt} &= F_T(C_{BP} - C_v) + PS(C_{int} - C_v) \\
\frac{dC_{int}}{dt} &= -PS(C_{int} - C_v) - k_{on} C_{int}(\tilde{R}_0 - C_b) + k_{off} C_b \\
\frac{dC_b}{dt} &= k_{on} C_{int}(\tilde{R}_0 - C_b) - k_{off} C_b - k_{intern} C_b \\
\frac{dC_{intern}}{dt} &= k_{intern} C_b - k_{rel} C_{intern}
\end{aligned}
$$

where

$$
C_{BP} = \frac{N_{BP}}{V_{BP}}, \quad C_v = \frac{N_v}{V_v}, \quad C_{int} = \frac{N_{int}}{V_{int}}, \quad C_b = \frac{N_b}{V_{int}}, \quad C_{intern} = \frac{N_{intern}}{V_{int}}, \quad \tilde{R}_0 = \frac{R_0}{V_{int}}
$$

Now we do a time scale separation analysis by the following change of time scale

$$
\tau = \epsilon t
$$

where ϵ is of the same order of the slowest varying parameters which are $\lambda_{bio}, k_{intern}$ and k_{rel}. For the new time scale we will have

$$
\frac{d}{dt} = \epsilon \frac{d}{d\tau}.
$$

Considering the fact that $\lambda_{bio}, k_{intern}$, and k_{rel} are of the same order as ϵ, the new system of ODEs will be:

$$
\begin{aligned}
\frac{dC_{BP}}{d\tau} &= -\epsilon \lambda_{bio} C_{BP}, \\
\frac{dC_b}{dt} &= \epsilon(k_{on} C_{int}(\tilde{R}_0 - C_b) - k_{off} C_b - k_{intern} C_b) \\
\frac{dC_{intern}}{dt} &= \epsilon(k_{intern} C_b - k_{rel} C_{intern})
\end{aligned}
$$

along with three algebraic equations for the quasi-steady-state approximation

$$
F_T(C_{BP} - C_v) + PS(C_{int} - C_v) = 0, \qquad -PS(C_{int} - C_v) - k_{on} C_{int}(\tilde{R}_0 - C_b) + k_{off} C_b = 0.
$$

Solving the system of equations above we will get

$$
C_v = \frac{C_{BP} C_b F_T k_{\text{on}} - C_{BP} F_T PS - C_{BP} F_T \tilde{R}_0 k_{\text{on}} - C_b PS k_{\text{off}}}{C_b F_T k_{\text{on}} + C_b PS k_{\text{on}} - F_T PS - F_T \tilde{R}_0 k_{\text{on}} - PS \tilde{R}_0 k_{\text{on}}},
$$

$$
C_{int} = \frac{-C_{BP} F_T PS - C_b F_T k_{\text{off}} - C_b PS k_{\text{off}}}{C_b F_T k_{\text{on}} + C_b PS k_{\text{on}} - F_T PS - F_T \tilde{R}_0 k_{\text{on}} - PS \tilde{R}_0 k_{\text{on}}}.
$$

Instead of having two sets of equations to track radioactive (hot) and and non-radioactive (cold) radiopharmaceuticals separately, we use a decaying exponential to calculate the number hot molecules at each timepoint in the tumour compartments. This approach works because the hot and cold radiopharmaceuticals are well mixed and we are always in a scenario where the mean number of hot molecules is a reasonable approximation of the underlying stochastic process.

Let $N_T(t)$ represent the total number of radiopharmaceuticals in the tumour tissue across all compartments at time t. Assuming that at the time of injection, the initial specific activity, defined as the ratio of hot radiopharmaceuticals to the total number of radiopharmaceuticals, is $f^H(0)$, and assuming the system is well-mixed, then the time dependent specific activity is given by

$$f^H(t) = f^H(0)e^{-\lambda_{phys}t}$$

where λ_{phys} is the decay rate constant. At any given time t the number of hot molecules in the tumour will be $N_H(t) = f^H(t) \times N_T(t)$ from which we can calculate the activity A followed by the dose rate ($\dot{D}$) to be used for the radiobiology model.

The survival model for tumour cells is based on the generalized Linear-Quadratic (LQ) model, which gives the survival probability of cells as a function of the delivered dose. The model incorporates the Lea-Catcheside factor to account for the repair of sublethal damage over time.

$$\textit{Survival Probability} = S = e^{-\alpha D - \beta G D^2}$$

where α and β are parameters for linear and quadratic part of LQ, D is the delivered dose and G is the Lea-Catcheside factor defined as below:

$$G = \frac{2}{D^2} \int_0^{t_{max}} \dot{D}(t) \left[\int_0^t \dot{D(t')} \exp\left(-\mu(t-t')\right) \, dt' \right] dt$$

where t_{max} is the irradiation time and μ is the repair rate. The value of t_{max} in the model is the time the cell has been exposed to radiation since its birth, and it is calculated for each cell individually based on its birth time.

The value of the parameter needed for this part are listed below. The values of these parameters are adopted from [13].

parameters	value in physical units	value in model units	model units
association rate k_{on}	$7.7 \times 10^{-1} ml/nmol/s$	3.465×10^{11}	$L^3/Q/T$
dissociation rate k_{off}	$7.7 \times 10^{-4}\ 1/s$	2.77	$1/T$
internalization rate k_{int}	$1.67 \times 10^{-5}\ 1/s$	6.01×10^{-2}	$1/T$
release rate k_{rel}	$2.67 \times 10^{-6}\ 1/s$	9.61×10^{-3}	$1/T$
decay rate Lu_{177}	$1.19 \times 10^{-6}\ 1/s$	4.28^{-3}	$1/T$

0.4 Lea-Catcheside Factor Derivation

The G-factor also known as the Lea-Catcheside factor is an important factor in radiobiology that incorporates the exposure pattern and the repair process into the cellular response models. This parameter quantifies the reduction in effective delivered dose due to cellular repair processes and the change due to different dose rates of exposure.

The derivation of the G-factor as derived from the work presented by Henkelman et al. [14], starts with the concept of accumulated effective dose, first introduced by Lea in 1938 [15]. This concept was further developed by Lajtha and Oliver in 1961, who proposed that the biological effect of a radiation dose delivered over time diminishes due to the repair of sublethal damage [16].

Cellular repair behavior during irradiation can be modelled as an exponential effect over time, where each dose is weighted exponentially based on its delivery time. Lea, DE and Catcheside, DG in 1942 formalize this phenamenon and named it as Lea-Catcheside G-factor [17] [18].

This weighting reflects the cellular repair dynamics, indicating that earlier doses have a small impact on effective dose calculations by the end of the irradiation interval. This occurs because cells have more time to repair earlier damages, whereas doses delivered later in the interval allow less time for cellular repair processes. As such, instead of having the accumulated dose at each time during the interval as:

$$D(t) = \int_0^t \dot{D(t')}\ dt'$$

We include the effect of repair as the exponential correction in the dose calculation. We define the accumulated effective dose D_{eff} as:

$$D_{eff}(t) = \int_0^t \dot{D(t')} \exp\left(-\mu(t-t')\right)\ dt'$$

μ is the repair rate of the cells. Now if we calculate the survival fraction of the cells at the end of the interval, we need the accumulated effective dose, D_{eff}. Assume survival fraction as a function of Dose is represented as f. So from the fundamental theorem of calculus it can be expressed as:

$$\ln(f(t_{max})) = \int_0^{t_{max}} \frac{\partial \ln f}{\partial D}\bigg|_{D_{eff}(t)} \dot{D}(t)\ dt$$

Replacing D_{eff} into the later equation, assuming survival fraction follows a Poissonian distribution like LQ model, $f(D) = e^{-\alpha D - \beta D^2}$ we get:

$$\ln f\bigg|_{t_{max}} = \ln f\bigg|_{D=D_{eff}} = \int_0^{t_{max}} \Big(-\alpha - 2\beta D_{eff} \Big) \dot{D}(t)\ dt$$

$$\ln f\bigg|_{t_{max}} = \int_0^{t_{max}} \Bigg(-\alpha - 2\beta \Bigg[\int_0^t \dot{D(t')} \exp\left(-\mu(t-t')\right)\ dt' \Bigg] \Bigg) \dot{D}(t)\ dt$$

$$= \int_0^{t_{max}} -\alpha \dot{D}(t)\ dt - \int_0^{t_{max}} 2\beta \Bigg[\int_0^t \dot{D(t')} \exp\left(-\mu(t-t')\right)\ dt' \Bigg] \dot{D}(t)\ dt$$

$$= -\alpha D - \beta 2 \int_0^{t_{max}} \dot{D}(t) \Bigg[\int_0^t \dot{D(t')} \exp\left(-\mu(t-t')\right)\ dt' \Bigg]\ dt$$

So the formula can be expressed as:

$$\ln f\bigg|_{t_{max}} = -\alpha D - \beta G D^2$$

Where $D = \int_0^{t_{max}} \dot{D}\, dt$ and G is the protraction factor (for the case that during the interval we had a continuous irradiation from time 0 to t_{max}), called "Lea-Catcheside factor" as:

$$G = \frac{2}{D^2} \int_0^{t_{max}} \dot{D}(t) \left[\int_0^t \dot{D(t')} \exp\left(-\mu(t-t')\right)\, dt' \right] dt$$

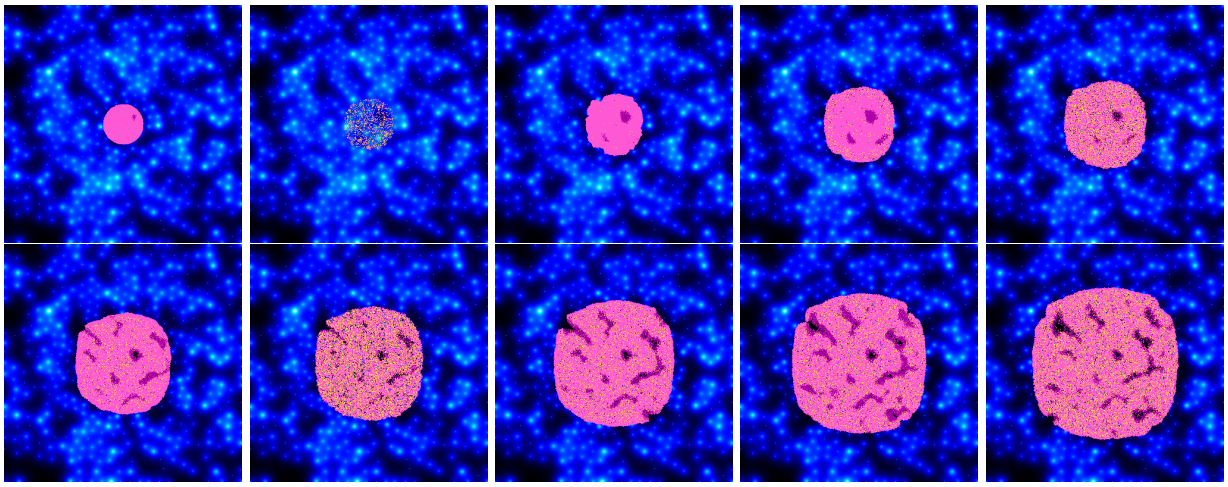

Figure S2: Effect of therapy 1 on the tumor with uniform vasculature with 0.3 removal probability shown at days 0, 12, 24, 36, and 48 (top row) and at days 60, 72, 84, 96, and 108 (bottom row). Normal tumor cells are shown in pink, hypoxic tumor cells in purple, necrotic tumor cells in gray, and apoptotic cells in yellow. The blue gradient indicates oxygen concentration, and the black background represents healthy tissue.

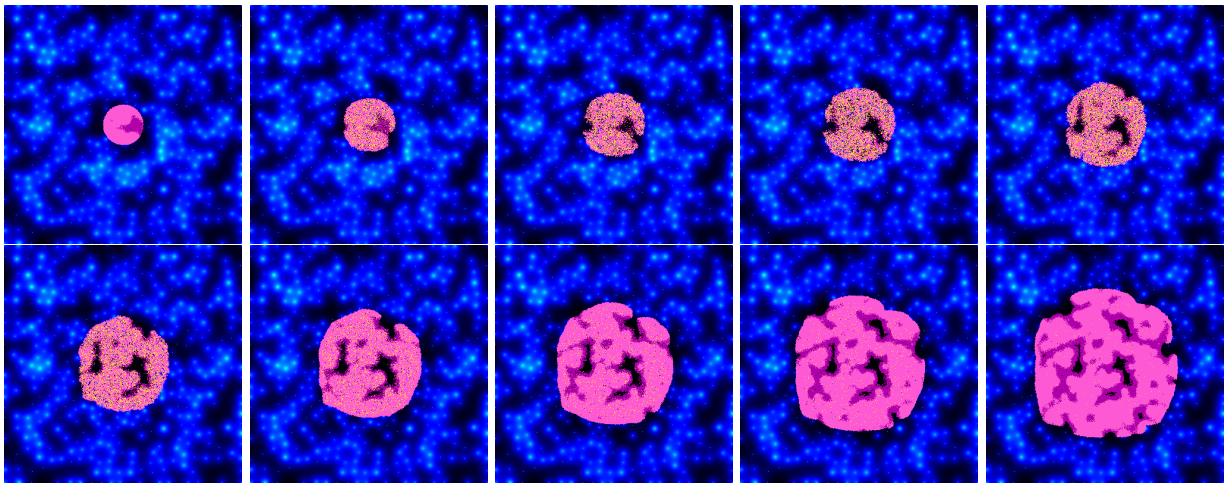

Figure S3: Effect of therapy 2 on the tumor with uniform vasculature with 0.3 removal probability shown at days 0, 12, 24, 36, and 48 (top row) and at days 60, 72, 84, 96, and 108 (bottom row). Normal tumor cells are shown in pink, hypoxic tumor cells in purple, necrotic tumor cells in gray, and apoptotic cells in yellow. The blue gradient indicates oxygen concentration, and the black background represents healthy tissue.

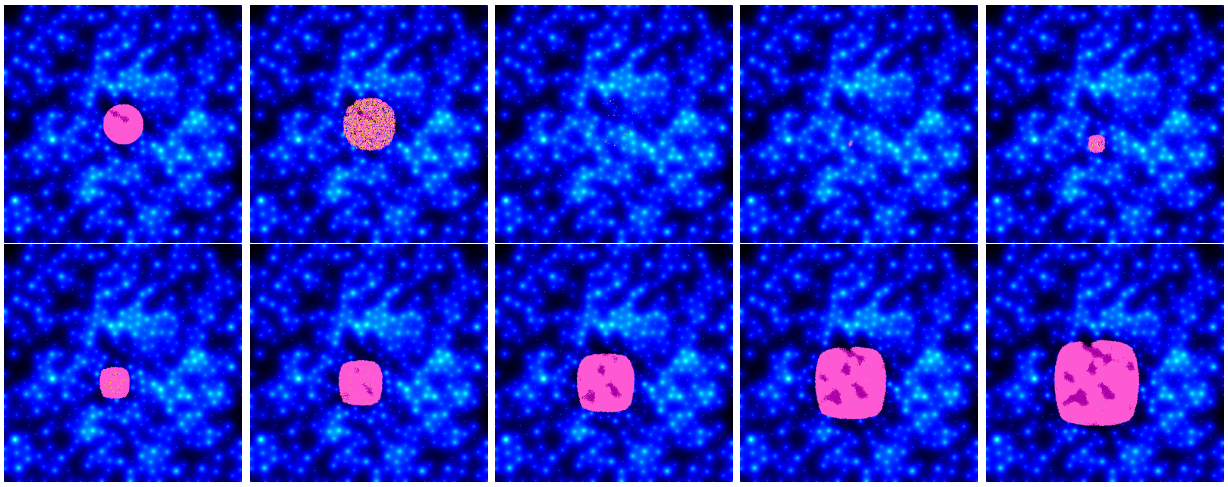

Figure S4: Effect of therapy 3 on the tumor with uniform vasculature with 0.3 removal probability shown at days 0, 12, 24, 36, and 48 (top row) and at days 60, 72, 84, 96, and 108 (bottom row). Normal tumor cells are shown in pink, hypoxic tumor cells in purple, necrotic tumor cells in gray, and apoptotic cells in yellow. The blue gradient indicates oxygen concentration, and the black background represents healthy tissue.

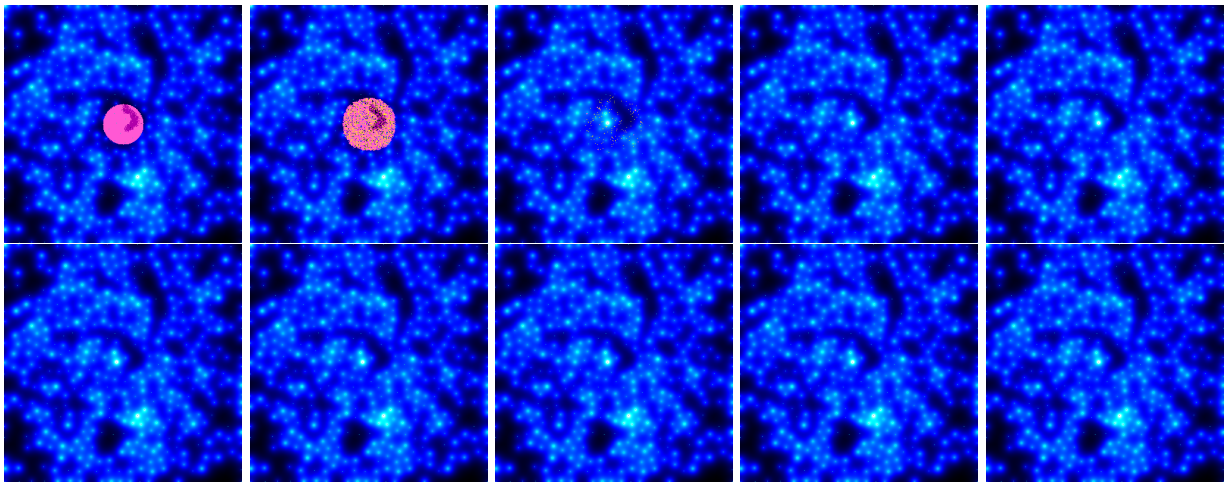

Figure S5: Effect of therapy 4 on the tumor with uniform vasculature with 0.3 removal probability shown at days 0, 12, 24, 36, and 48 (top row) and at days 60, 72, 84, 96, and 108 (bottom row). Normal tumor cells are shown in pink, hypoxic tumor cells in purple, necrotic tumor cells in gray, and apoptotic cells in yellow. The blue gradient indicates oxygen concentration, and the black background represents healthy tissue.

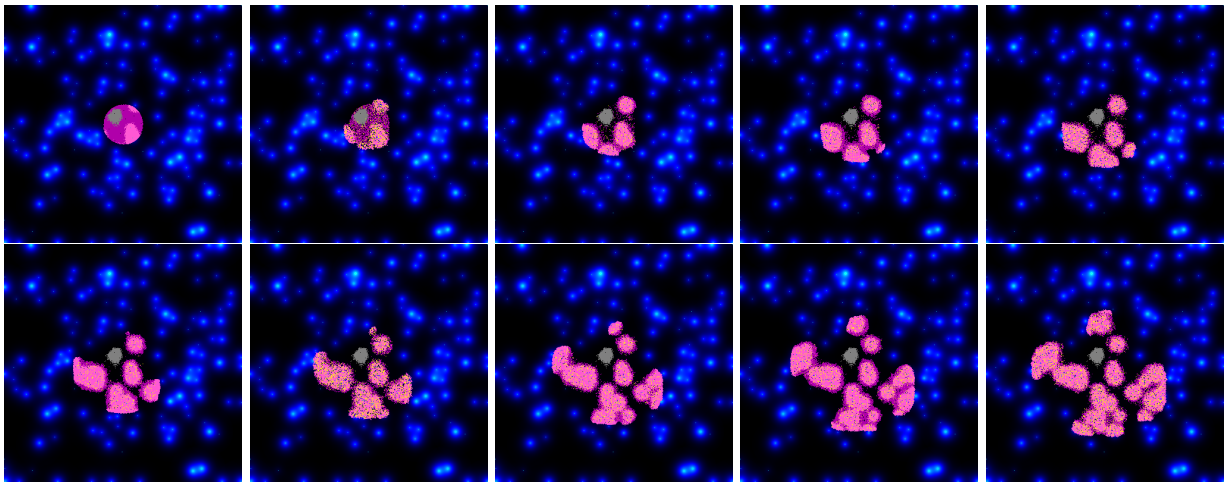

Figure S6: Effect of therapy 1 on the tumor with uniform vasculature with 0.8 removal probability shown at days 0, 12, 24, 36, and 48 (top row) and at days 60, 72, 84, 96, and 108 (bottom row). Normal tumor cells are shown in pink, hypoxic tumor cells in purple, necrotic tumor cells in gray, and apoptotic cells in yellow. The blue gradient indicates oxygen concentration, and the black background represents healthy tissue.

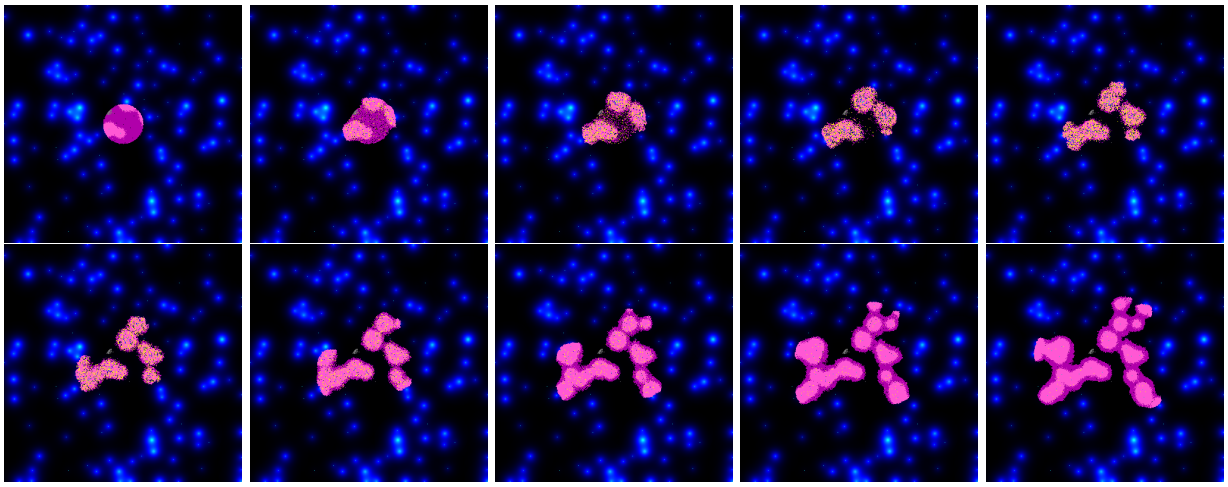

Figure S7: Effect of therapy 2 on the tumor with uniform vasculature with 0.8 removal probability shown at days 0, 12, 24, 36, and 48 (top row) and at days 60, 72, 84, 96, and 108 (bottom row). Normal tumor cells are shown in pink, hypoxic tumor cells in purple, necrotic tumor cells in gray, and apoptotic cells in yellow. The blue gradient indicates oxygen concentration, and the black background represents healthy tissue.

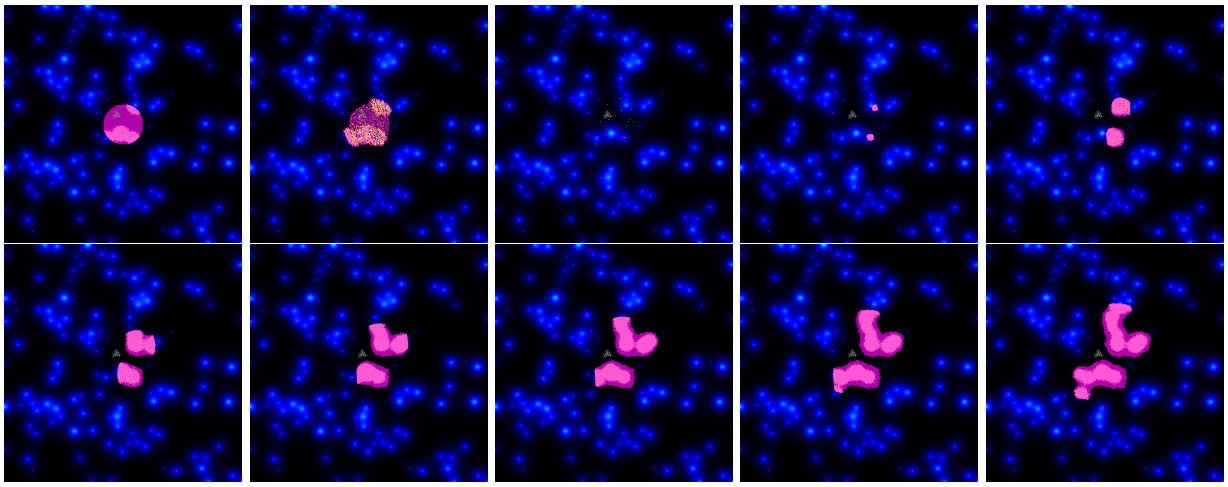

Figure S8: Effect of therapy 3 on the tumor with uniform vasculature with 0.8 removal probability shown at days 0, 12, 24, 36, and 48 (top row) and at days 60, 72, 84, 96, and 108 (bottom row). Normal tumor cells are shown in pink, hypoxic tumor cells in purple, necrotic tumor cells in gray, and apoptotic cells in yellow. The blue gradient indicates oxygen concentration, and the black background represents healthy tissue.

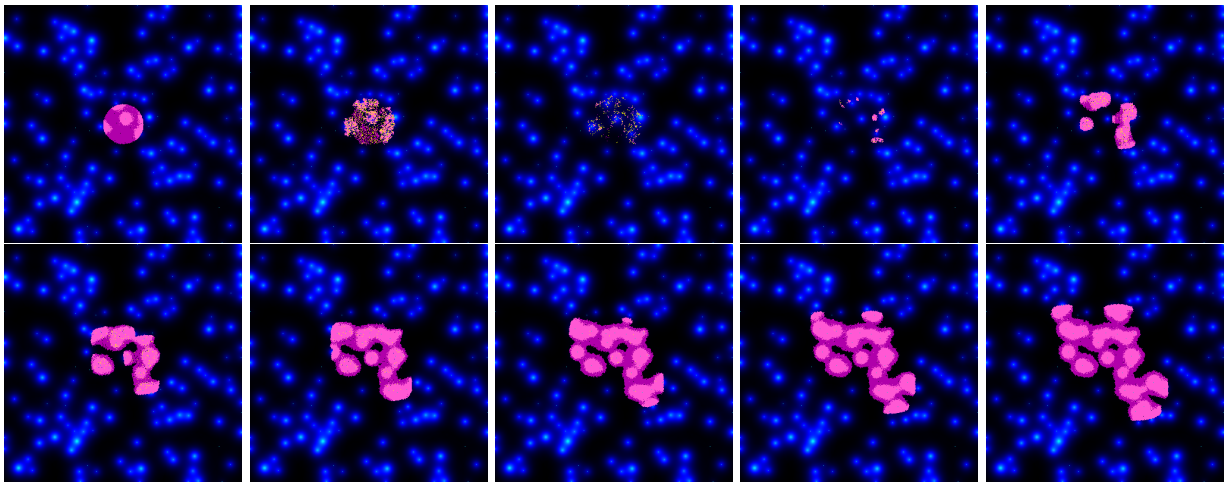

Figure S9: Effect of therapy 4 on the tumor with uniform vasculature with 0.8 removal probability shown at days 0, 12, 24, 36, and 48 (top row) and at days 60, 72, 84, 96, and 108 (bottom row). Normal tumor cells are shown in pink, hypoxic tumor cells in purple, necrotic tumor cells in gray, and apoptotic cells in yellow. The blue gradient indicates oxygen concentration, and the black background represents healthy tissue.

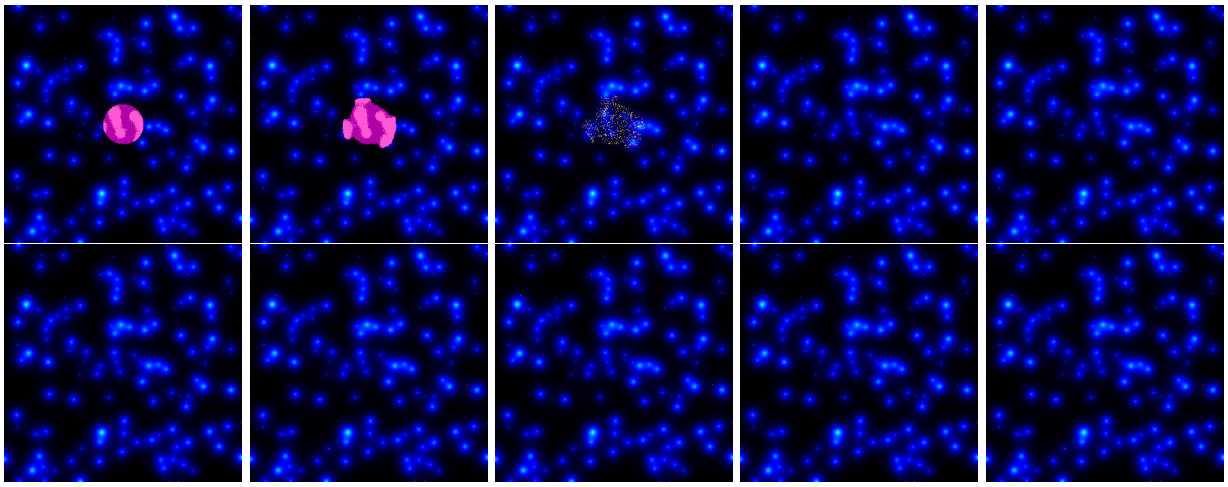

Figure S10: Effect of therapy 5 on the tumor with uniform vasculature with 0.8 removal probability shown at days 0, 12, 24, 36, and 48 (top row) and at days 60, 72, 84, 96, and 108 (bottom row). Normal tumor cells are shown in pink, hypoxic tumor cells in purple, necrotic tumor cells in gray, and apoptotic cells in yellow. The blue gradient indicates oxygen concentration, and the black background represents healthy tissue.

References

[1] J Martin Brown and William R Wilson. Exploiting tumour hypoxia in cancer treatment. *Nature Reviews Cancer*, 4(6):437–447, 2004.

[2] Peter Vaupel, Michael Höckel, and Arnulf Mayer. Detection and characterization of tumor hypoxia using po2 histography. *Antioxidants & redox signaling*, 9(8):1221–1236, 2007.

[3] JL Tatum, GJ Kelloff, RJ Gillies, JM Arbeit, JM Brown, KS Chao, JD Chapman, WC Eckelman, AW Fyles, AJ Giaccia, et al. Hoff man j, liu g, stone h, sullivan d. hypoxia: importance in tumor biology, noninvasive measurement by imaging, and value of its measurement in the management of cancer therapy. *Int J Radiat Biol*, 82:699–757, 2006.

[4] Thomas K Goldstick, Vincent T Ciuryla, and Leon Zuckerman. Diffusion of oxygen in plasma and blood. In *Oxygen transport to tissue—ii*, pages 183–190. Springer, 1976.

[5] Timothy J Strovas, Sarah C McQuaide, Judy B Anderson, Vivek Nandakumar, Marina G Kalyuzhnaya, Lloyd W Burgess, Mark R Holl, Deirdre R Meldrum, and Mary E Lidstrom. Direct measurement of oxygen consumption rates from attached and unattached cells in a reversibly sealed, diffusionally isolated sample chamber. *Advances in bioscience and biotechnology (Print)*, 5(5):398, 2010.

[6] Ioanna Papandreou, Rob A Cairns, Lucrezia Fontana, Ai Lin Lim, and Nicholas C Denko. Hif-1 mediates adaptation to hypoxia by actively downregulating mitochondrial oxygen consumption. *Cell metabolism*, 3(3):187–197, 2006.

[7] Brett A Wagner, Sujatha Venkataraman, and Garry R Buettner. The rate of oxygen utilization by cells. *Free Radical Biology and Medicine*, 51(3):700–712, 2011.

[8] Juan A Delgado-SanMartin, Jennifer I Hare, Alessandro PS de Moura, and James WT Yates. Oxygen-driven tumour growth model: a pathology-relevant mathematical approach. *PLOS Computational Biology*, 11(10):e1004550, 2015.

[9] Jiacun Wang. *Formal methods in computer science*. Chapman and Hall/CRC, 2019.

[10] Peter Vaupel, Ann Barry Flood, and Harold M Swartz. Oxygenation status of malignant tumors vs. normal tissues: Critical evaluation and updated data source based on direct measurements with po2 microsensors. *Applied Magnetic Resonance*, 52(10):1451–1479, 2021.

[11] Aurélie Gomes, Ludivine Guillaume, David Robert Grimes, Jérôme Fehrenbach, Valérie Lobjois, and Bernard Ducommun. Oxygen partial pressure is a rate-limiting parameter for cell proliferation in 3d spheroids grown in physioxic culture condition. *PloS one*, 11(8):e0161239, 2016.

[12] Ashlyn G Rickard, Gregory M Palmer, and Mark W Dewhirst. Clinical and pre-clinical methods for quantifying tumor hypoxia. *Hypoxia and Cancer Metastasis*, pages 19–41, 2019.

[13] Gabriele Birindelli, Milos Drobnjakovic, Volker Morath, Katja Steiger, Calogero D'Alessandria, Eleni Gourni, Ali Afshar-Oromieh, Wolfgang Weber, Axel Rominger, Matthias Eiber, and Kuangyu Shi. Is hypoxia a factor influencing PSMA-Directed radioligand Therapy?-An in silico study on the role of chronic hypoxia in prostate cancer. *Cancers*, 13(14), July 2021.

[14] R M Henkelman, G K Lam, R O Kornelsen, and C J Eaves. Explanation of dose-rate and split-dose effects on mouse foot reactions using the same time factor. *Radiat. Res.*, 84(2):276–289, November 1980.

[15] D E Lea. A theory of the action of radiations on biological materials capable of recovery part 1. *Br. J. Radiol.*, 11(127):489–497, July 1938.

[16] L G Lajtha and R Oliver. Some radiobiological considerations in radiotherapy. *Br. J. Radiol.*, 34:252–257, April 1961.

[17] DE Lea and DG Catcheside. The mechanism of the induction by radiation of chromosome aberrations in tradescantia. *Journal of genetics*, 44:216–245, 1942.

[18] David J Brenner. The linear-quadratic model is an appropriate methodology for determining isoeffective doses at large doses per fraction. In *Seminars in radiation oncology*, volume 18, pages 234–239. Elsevier, 2008.